High-resolution hard x-ray magnetic imaging with dichroic ptychography

Claire Donnelly,[1,2] Valerio Scagnoli,[1,2,*] Manuel Guizar-Sicairos,[2] Mirko Holler,[2] Fabrice Wilhelm,[3] Francois Guillou,[3] Andrei Rogalev,[3] Carsten Detlefs,[3] Andreas Menzel,[2] Jörg Raabe,[2] and Laura J. Heyderman[1,2]

[1]*Laboratory for Mesoscopic Systems, Department of Materials, ETH Zurich, 8093 Zurich, Switzerland*
[2]*Paul Scherrer Institute, 5232 Villigen PSI, Switzerland*
[3]*ESRF, 71 Avenue des Martyrs, 38000 Grenoble, France*

Imaging the magnetic structure of a material is essential to understanding the influence of the physical and chemical microstructure on its magnetic properties. Magnetic imaging techniques, however, have been unable to probe three-dimensional micrometer-size systems with nanoscale resolution. Here we present the imaging of the magnetic domain configuration of a micrometer-thick FeGd multilayer with hard x-ray dichroic ptychography at energies spanning both the Gd L_3 edge and the Fe K edge, providing a high spatial resolution spectroscopic analysis of the complex x-ray magnetic circular dichroism. With a spatial resolution reaching 45 nm, this advance in hard x-ray magnetic imaging is a first step towards the investigation of buried magnetic structures and extended three-dimensional magnetic systems at the nanoscale.

For optimal integration of new magnetic materials and systems into technological applications, a detailed understanding of the magnetic structure and properties is required. In particular, for the next generation of nanocomposite permanent magnets, which have the potential to enable more efficient, smaller, and lighter energy harvesters and motors [1], an understanding of the influence of the physical and chemical microstructure on the magnetic configurations is of the utmost importance. X-ray imaging is an excellent candidate for such investigations [2,3], offering high spatial resolution, element specificity, high sensitivity, and the ability to directly and nondestructively probe the magnetization of a material. However, so far, all submicrometer spatial resolution x-ray magnetic imaging has been performed with soft x rays, with photon energies below 1.6 keV, due to the strong magnetic signal available in this regime [4,5]. While effective for probing the magnetism of thin films and nanostructures [4,6], soft x rays are limited to systems with total material thickness below approximately 200 nm [7,8]. Neutron magnetic imaging allows the study of systems with thicknesses ranging from micrometers up to millimeters, but only with a spatial resolution of tens to hundreds of micrometers [9–12]. As a result, high spatial resolution magnetic investigations of thick permanent magnets to be used in microsystems such as electromagnetic sensors and energy harvesting devices [13–15], as well as the study of buried structures integrated into, for example, silicon-based devices [16], have not been possible.

Higher-energy x rays offer a solution to such limitations, with recent advances providing nanometer spatial resolution imaging of structures with thickness on the order of many micrometers [17]. For magnetic imaging, however, hard x rays have not been considered to be competitive. Indeed, soft x rays, by utilizing the $L_{2,3}$ edges ($2p \rightarrow 3d$) of transition metals and the $M_{4,5}$ edges ($3d \rightarrow 4f$) of rare earths, directly probe the valence band of the magnetic material. In the hard x-ray regime, however, one indirectly probes the magnetization at the $K(1s \rightarrow 4p)$ edges of transition metals and the $L_{2,3}$

$(2p \rightarrow 5d)$ edges of rare earths, resulting in a significantly weaker magnetic signal [18]. To the best of our knowledge, in previous studies of hard x-ray magnetic imaging, a maximum spatial resolution of 2 μm has been reached for the imaging of two-dimensional objects [19–22].

Here we present hard x-ray magnetic imaging at the nanoscale with a spatial resolution of 45 nm. As a proof of principle, we image the magnetic domain configuration of a micrometer-thick FeGd film at energies spanning not only the Gd L_3 edge, with relatively strong magnetic contrast, but also the Fe K edge. While the magnetic signal is substantially weaker at the Fe K edge, we demonstrate that we can image the magnetic configuration of the Fe within the system, thus demonstrating the applicability of the technique to non-rare-earth magnetic elements, which are of scientific interest as an important alternative to the scarce and expensive rare-earth magnetic materials [23]. We perform a quantitative spectroscopic analysis of the full complex transmission function for energies spanning the Gd L_3 edge, providing a detailed insight into the relationship between the phase and absorption x-ray magnetic circular dichroism (XMCD) signals and confirming the quantitative nature of the technique. Furthermore, we measure the magnetic configuration of a film with a thickness of 500 nm, therefore demonstrating the potential of the technique to investigate thinner films. With hard x-ray magnetic imaging with nanoscale resolution, the investigation of magnetic configurations of a wide range of samples is now possible.

In order to measure the weak magnetic signals in the hard x-ray regime, a high level of sensitivity is required, which is provided by ptychography. Ptychography is a scanning coherent diffractive imaging technique, which gives access to the full complex transmission function of an object [24,25]. The sample is illuminated with a coherent beam, and far-field diffraction patterns are measured for many overlapping illumination positions. Both the object and illumination functions are then retrieved using an iterative reconstruction algorithm [25–27]. When combined with three-dimensional imaging techniques such as tomography, this access to the full complex transmission function provides a means to obtain a

---

*valerios@ethz.ch

three-dimensional mapping of the electron [17,28] and atomic densities [29] within a sample.

When applied to magnetic imaging, coherent diffractive imaging (CDI) techniques such as ptychography offer high-resolution imaging with a number of key advantages [4,30–34]. For instance, the complex magnetic signal provided by both CDI and ptychography makes possible the imaging of ferromagnetic domains with linearly polarized light. Here the magnetic diffraction is isolated by subtracting the pure electronic scattering measured when the magnetic state is removed with a saturating magnetic field [30,32]. In an investigation of the complex magnetic signal with soft x-ray holography, it was reported that phase imaging before the absorption edge can minimize the radiation dose required [31].

In this work, we combine ptychography with x-ray magnetic circular dichroism (XMCD) in the hard x-ray regime. In particular, we study FeGd multilayers, which are amorphous films with perpendicular magnetic anisotropy. XMCD is a resonant effect that occurs when the photon energy is tuned close to an atomic absorption edge. The electronic transitions between the resonant core level and the magnetically polarized valence band then become sensitive to the helicity of the x rays and the projection of the sample's magnetization along the beam direction. Experiments are typically performed by reversing the x-ray helicity and/or the sample magnetization. A more in-depth description of XMCD is given by, for example, Ref. [2]. In the case of ptychography, it is crucial to have a clear understanding of the complex index of refraction resulting from the interactions between the sample and the x rays, especially when dichroic and birefringent effects cannot be neglected, as in XMCD. In particular, the assumption in standard ptychography that the probe and object are complex functions that interact via a scalar product may not hold [35].

For the case of x rays interacting with a magnetic material, one must consider both the electronic and magnetic contributions to the scattering factor [36–38]:

$$
f = f_c(\boldsymbol{\epsilon}_f^* \cdot \boldsymbol{\epsilon}_i) - i f_m^{(1)}(\boldsymbol{\epsilon}_f^* \times \boldsymbol{\epsilon}_i) \cdot \mathbf{m}(\mathbf{r}) \\
+ f_m^{(2)}(\boldsymbol{\epsilon}_f^* \cdot \mathbf{m}(\mathbf{r}))(\boldsymbol{\epsilon}_i \cdot \mathbf{m}(\mathbf{r})),
\tag{1}
$$

where $\mathbf{m}$ is the magnetization vector, $\boldsymbol{\epsilon}_i$ and $\boldsymbol{\epsilon}_f$ are the Jones polarization vectors of the incoming and scattered waves, respectively, $*$ denotes complex conjugation, and f_c, $f_m^{(1)}$, and $f_m^{(2)}$ are the complex-valued charge, circular, and linear dichroic magnetic scattering factors, respectively. For the case of small angle scattering, and under the approximation of perfectly circularly polarized incoming photons and a nonbirefringent interaction, as is the case for the amorphous film studied in this work, Eq. (1) is reduced to

$$
f = f_c - i f_m^{(1)} \begin{pmatrix} \boldsymbol{\epsilon}_{C_R}^* \times \boldsymbol{\epsilon}_{C_R} & \boldsymbol{\epsilon}_{C_L}^* \times \boldsymbol{\epsilon}_{C_R} \\ \boldsymbol{\epsilon}_{C_R}^* \times \boldsymbol{\epsilon}_{C_L} & \boldsymbol{\epsilon}_{C_L}^* \times \boldsymbol{\epsilon}_{C_L} \end{pmatrix} \cdot \mathbf{m}(\mathbf{r}) \\
= f_c - i f_m^{(1)} \begin{pmatrix} i m_z & 0 \\ 0 & -i m_z \end{pmatrix}.
\tag{2}
$$

For circularly right (C_R) and left (C_L) polarized incident light, there are therefore two nonzero matrix elements for the second term in Eq. (2): the C_L-to-C_L and the C_R-to-C_R scattering channels, which are equal to $\pm f_m^{(1)} m_z$, where m_z is the component of the magnetization along the propagation direction.

The contribution of $f_m^{(2)}$ has been neglected as both scalar products are approximately zero for the case of circularly polarized light and perpendicular magnetic anisotropy, where the magnetization and polarization vectors are perpendicular. The latter term in Eq. (2) is then the source of the XMCD signal that we probe with dichroic ptychography, and the result on the outgoing wave is a scalar addition to the scattering factor, which effectively results in a modification to the phase shift and amplitude of the outgoing wave.

In considering a formalism for the ptychographic reconstructions, it is apparent that there are no polarization cross terms representing, for example, C_R-to-C_L scattering channels between different polarizations. We can therefore conclude that for the case of perfectly circularly polarized incident light, the standard assumption that the probe and the object are complex functions that interact via a scalar product is valid. The interaction can be then expressed as in conventional ptychography as

$$
\boldsymbol{\Psi}_j(\mathbf{r}) = \mathbf{P}(\mathbf{r})\mathbf{O}(\mathbf{r} - \mathbf{r}_j),
\tag{3}
$$

where $\boldsymbol{\Psi}_j(\mathbf{r})$ is the exit field after the sample, $\mathbf{P}(\mathbf{r})$ is the incident illumination, and $\mathbf{O}(\mathbf{r} - \mathbf{r}_j)$ is the transmissivity of the sample, which can be expressed in terms of the scattering factors as follows:

$$
\mathbf{O}(\mathbf{r} - \mathbf{r}_j) = \exp\left\{ i \frac{\omega}{c} \int \left[1 - \frac{r_e}{2\pi} \lambda^2 n_{\mathrm{at}} f(\mathbf{r} - \mathbf{r}_j) \right] dz \right\},
\tag{4}
$$

$\boldsymbol{\Psi}_j(\mathbf{r})$, $\mathbf{P}_j(\mathbf{r})$, and $\mathbf{O}(\mathbf{r} - \mathbf{r}_j)$ are all complex-valued functions of $\mathbf{r}$ which are the transverse Cartesian coordinates, and j indicates the ptychography scan position. Here ω is the frequency of the x rays, c is the speed of light, r_e is the classical electron radius, λ is the wavelength of the x rays, n_{at} is the atomic density of a particular element, and $f(\mathbf{r} - \mathbf{r}_j)$ is the scattering factor [defined in Eq. (1)].

Experimentally, we perform ptychography scans with C_L and C_R polarized light in order to nondestructively image magnetic features in our sample with both phase and absorption magnetic contrast, without the need to apply a saturating field. Explicitly, the complex transmission function is given by $T(E) = a(E)e^{i\phi(E)}$, where a is the amplitude and ϕ the phase, which both depend strongly on the x-ray energy E in the vicinity of an absorption edge. We define the dichroic signal as

$$
A_{\mathrm{XMCD}}(\%) = (|a_{\mathrm{L}}|^2 - |a_{\mathrm{R}}|^2)/\Delta_{\mathrm{edge}} \times 100\%,
\tag{5}
$$

$$
\phi_{\mathrm{XMCD}} = \phi_{\mathrm{L}} - \phi_{\mathrm{R}},
\tag{6}
$$

where A_{XMCD} and ϕ_{XMCD} are the absorption and phase XMCD signals, respectively, and Δ_{edge} is the relative change in absorption across the absorption edge. $a_{\mathrm{L,R}}$ and $\phi_{\mathrm{L,R}}$ are the amplitude and phase of the complex transmission function, respectively, measured with left (L) and right (R) circularly polarized incident light.

The dichroic ptychography setup (see Appendix C for more details) is shown in Fig. 1(a). In order to probe the XMCD, circularly polarized light was produced by converting linearly polarized light using a 500-μm-thick diamond quarter-wave phase retarder [39] and the degree of polarization of the x rays was determined using a polarization analyzer setup [40]. The x rays were found to be over 99% circularly polarized, with the phase plate absorbing approximately 65% of the incident light.
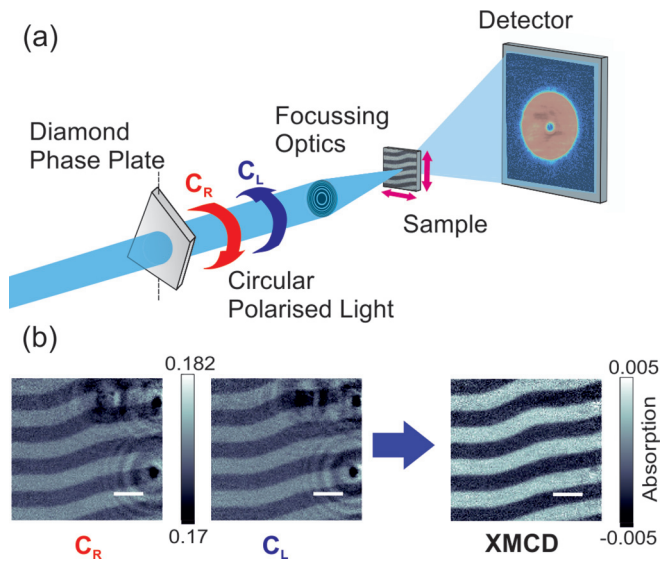
FIG. 1. (a) The dichroic ptychography setup. A diamond phase plate converts linearly polarized light into C_L or C_R light, which is then focused close to the sample plane. A piezoelectric stage is used to scan the sample across the beam. (b) The absorption part of reconstructed images taken with C_L and C_R polarized light at the Gd L_3 edge with a photon energy of 7.2445 keV, which contain both electron density and magnetic contributions. The difference of these images removes the electron density contrast of Pt reference structures on the sample to give a purely magnetic image, i.e., with XMCD contrast. Scale bars represent 1 μm.

Ptychography scans with a field of view of $5 \times 5 \ \mu\text{m}^2$ consisted of a diffraction pattern being measured at each of 278 scanning points placed on a Fermat spiral grid [41]. At each point, the diffraction pattern was measured with a 0.2 second exposure time using a single-photon counting Pilatus 2M detector [42,43] located 7.219(1) m downstream of the sample. Each scan took approximately 112 seconds, which includes the time taken for positioning the sample at each point with a piezoelectric motor. To enhance the signal-to-noise ratio, ten such scans were repeated for each energy, measured with left and right circularly polarized light.

Ptychographic reconstructions were performed using a gradient-based maximum-likelihood estimation [26,44] with a maximum possible number of iterations of 500, although convergence was typically reached before 300 iterations. Further details on the experimental setup and reconstruction are given in Appendices C and D.

Here we employ dichroic ptychography to image the magnetic configurations of 1-μm-thick and 500-nm-thick Fe(0.41 nm)/Gd(0.45 nm) multilayer films with perpendicular magnetic anisotropy. The multilayer films were deposited with RF magnetron sputtering on a Si_3N_4 membrane with a growth rate of 0.15 nm/s at room temperature and characterized as described in Appendix A. To enable easier image alignment, platinum nanostructures were deposited on the film with focused electron-beam deposition.

To demonstrate the isolation of the magnetic signal, the absorption part of the ptychography reconstructions taken with C_L and C_R polarized light at the Gd L_3 edge, with a photon energy of 7.2445 keV, are shown in Fig. 1(b). Along

with the electron density contrast of the platinum alignment structures, magnetic stripe domains are visible and the magnetic contrast reverses when the polarization is changed from C_L to C_R. The difference of the two images removes the electron density contrast, which in this case corresponds mainly to the platinum alignment structures, and results in an XMCD image with purely magnetic contrast, as shown in the rightmost image of Fig. 1(b).

The spatial resolution of a single absorption image was determined via Fourier ring correlation (FRC) [45] to be approximately 60 nm. Averaging of five images resulted in a spatial resolution of 45 nm, representing a 50-fold increase in the achieved spatial resolution with dichroic ptychography compared with previous measurements with hard x rays [19–22]. The spatial resolution of the phase images, however, was estimated to be 70–80 nm. Thus, while the phase information typically offers better electron density contrast, in our experiment absorption contrast provided better magnetic contrast and spatial resolution. The edge sharpness of the domain walls was found to be approximately 60 nm by taking a line profile of the image intensity across a domain wall and measuring the 10%–90% edge sharpness. It should be noted that thanks to recent advances in x-ray optics, which allow for the x-ray beam to be focused down to a 30 nm spot [46], a better resolution than that reported in Refs. [19–22] would, in principle, be possible with other techniques such as scanning transmission x-ray microscopy. However, to the best of our knowledge, such measurements have not been published.

To investigate the energy dependence of the complex XMCD signal and demonstrate the quantitative nature of the technique, dichroic ptychography was performed for different photon energies spanning the Gd L_3 edge, which ranged from 7.234 to 7.2565 keV in steps of 1.5 eV. Images of the phase and absorption components of the sample transmission are shown in Fig. 2(a). Below the edge, the magnetic phase contrast is inverted with respect to the absorption contrast and can be seen to reverse when traversing the absorption edge. To measure the phase and absorption XMCD signal, a Gaussian distribution was fitted to the histograms of the XMCD contrast of the pixels within the domains. This fit is performed for a number of separate domains, and the mean and standard deviation of the XMCD signal calculated. The phase and absorption XMCD signals are given as a function of energy across the absorption edge in Fig. 2(b), represented by blue squares (ϕ_{XMCD}) and red circles (A_{XMCD}), and the maximum absorption contrast is found to be 8.2% of Δ_{edge} at 7.2445 keV, 1 eV below the absorption edge.

To determine the most effective energy at which to image, both the radiation dose and the magnetic contrast must be optimized. A single projection delivered an x-ray radiation dose of 1.4 and 2.3 MGy on the sample just below the absorption edge at 7.240 keV and at the absorption edge at 7.2445 keV, respectively. Although phase imaging before the edge may therefore result in reduced radiation damage, the on-resonance A_{XMCD} signal is approximately four times higher. Therefore, for the same image contrast, less cumulative dose is delivered when measuring in absorption on-resonance with a shorter exposure time.

In order to confirm that the ptychography measurements provide a quantitative measurement of the complex XMCD
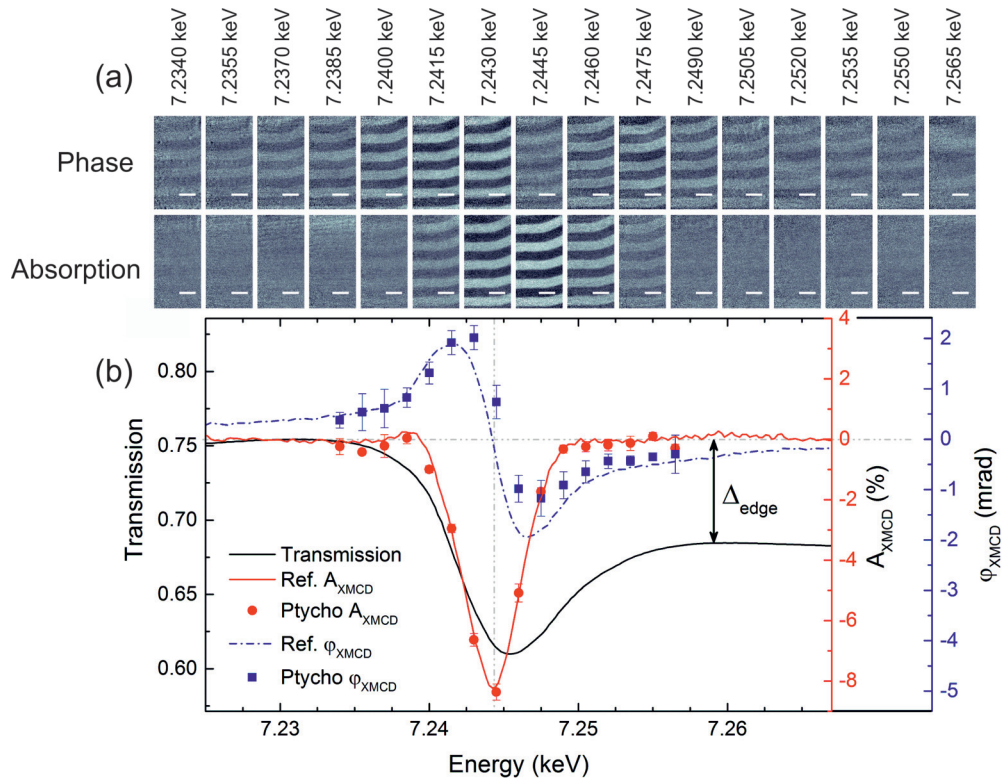
FIG. 2. (a) XMCD ptychographic images of the magnetic domain configuration of the FeGd film obtained from the difference taken between images measured with C_R and C_L polarized light. Phase (upper row) and absorption (lower row) contrast are given for a number of photon energies spanning the Gd L_3 edge. Scale bars represent 1 μm. (b) The A_{XMCD} (red circles) and ϕ_{XMCD} (blue squares) signal extracted from the images is presented, providing a direct comparison of the phase and absorption signals. The XMCD data are compared with a reference A_{XMCD} spectrum (red line) measured in fluorescence on a similar sample, and the corresponding ϕ_{XMCD} reference spectrum calculated with the Kramers-Kronig relations (dashed blue line). A transmission spectrum of the sample (black line) is provided as a reference.

signal, the ptychography A_{XMCD} spectrum was compared with a reference A_{XMCD} spectrum measured in fluorescence yield with a standard XMCD setup on an equivalent sample (see Appendix B for more details) [47], also plotted in Fig. 2(b) (red line). From the excellent agreement between the magnitude and form of the A_{XMCD} signals measured with ptychography and the fluorescence technique, it is evident that dichroic ptychography not only allows high-quality imaging of the domain structure with unprecedented spatial resolution and sensitivity, but moreover provides a quantitative measure of the magnetic contrast. This allows the relative magnitude of vector components of the magnetization to be directly compared, which is critical for three-dimensional magnetic investigations. The direct measurement of the ϕ_{XMCD} signal (blue squares) is further compared with a ϕ_{XMCD} spectrum calculated from reference absorption spectra using the Kramers-Kronig relations [18] (dashed blue line) in Fig. 2(b). While the calculated spectrum is symmetric about the inversion point, the measured ϕ_{XMCD} data is shifted by 0.5 eV, with the magnitude of its signal being asymmetric about the inversion point. Although not critical to the current work, these differences are likely to be associated with a physical effect that warrants further investigation in the future.

The element specificity of x rays enables the direct comparison of the magnetization of different elements within a sample. In the hard x-ray regime, the K edges of transition metals are also available, offering the possibility of studying magnetic materials beyond rare earths. Although the magnetic signal at the Fe K edge is an order of magnitude weaker than that found at the Gd L_3 edge [2], we are able to image the magnetic domains at a range of energies across the Fe K edge, demonstrating the sensitivity and quantitativeness of dichroic ptychography. The ptychography A_{XMCD} data extracted from the images measured at energies spanning the Fe K edge are shown in Fig. 3 (red squares). The spectrum is compared directly with a reference spectrum measured in fluorescence yield with a standard XMCD setup (red line), and a good level of agreement between the ptychography data and reference spectrum can be seen.

To compare the magnetization of the Fe and Gd within the sample, the same section of the domain structure was imaged at the Fe K edge and at the Gd L_3 edge. Magnetic absorption images measured with C_L polarized x rays are shown in Fig. 4, and the magnetic domains are highlighted with black and white arrows to the left of the images. As the XMCD signal found at the Fe K edge is approximately ten times weaker than that found at the Gd L_3 edge, the signal-to-noise ratio of the image measured at the Fe K edge is visibly weaker. On comparing the magnetic contrast measured at the Gd L_3 edge (left image) and the Fe K edge (right image), we observe the same domain structure that is reversed in contrast, indicating that the Fe and Gd are coupled antiferromagnetically as in the ferrimagnetic FeGd alloy [30].
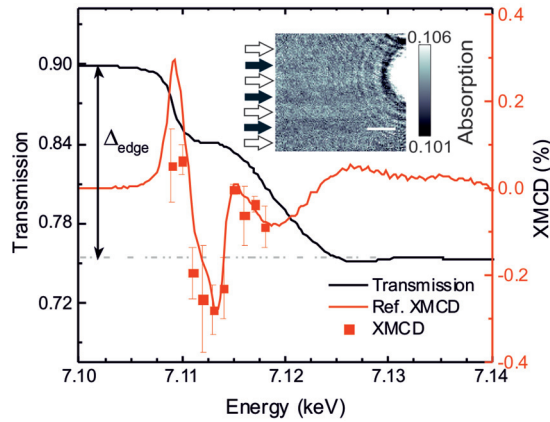
FIG. 3. The A_{XMCD} signal measured with dichroic ptychography across the Fe K edge (red squares) is plotted along with a reference XMCD spectrum (red line) measured in fluorescence on a similar film. A single polarization image is given in the inset, where the stripe domain pattern can be seen, along with the electron density contrast of the Pt markers. The domains are indicated by white and black arrows to the left of the image.

Finally, in order to investigate the suitability of hard x-ray ptychography for the imaging of thinner layers, the domain structure of a 500-nm-thick FeGd film was imaged at the Gd L_3 edge with a photon energy of 7.243 keV. The absorption image is shown in Fig. 5(a). The magnetic domains were found to have average widths of (390 ± 7) and (554 ± 11) nm for the 500-nm-thick and 1-μm-thick films, respectively. This is in good agreement with Kittel's prediction that the domain width of a thick film with uniaxial anisotropy will scale proportionally to the square root of the thickness of the film [48].

The effect of the strength of the XMCD signal on the spatial resolution was determined by comparing the spatial resolution of images of the 500-nm-thick film measured at the Gd L_3 edge [Fig. 5(a)] and the 1 μm film measured at the Fe K edge [Fig. 5(b)] with the 45 nm spatial resolution that was
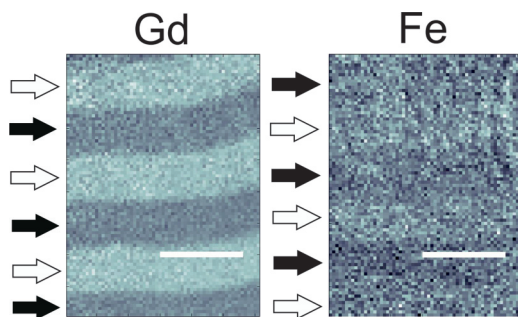

FIG. 4. Absorption images of the domain structure of FeGd, measured with C_L polarized light at the Gd L_3 edge with a photon energy of 7.2445 keV (left image) and the Fe K edge with a photon energy of 7.113 keV (right image). Domains of opposite magnetization are indicated by black and white arrows on the left-hand side of the images. The reversal in contrast between the Fe K edge and the Gd L_3 edge is an indication of the antiferromagnetic coupling between the Fe and Gd magnetic moments. The scale bars represent 1 μm.
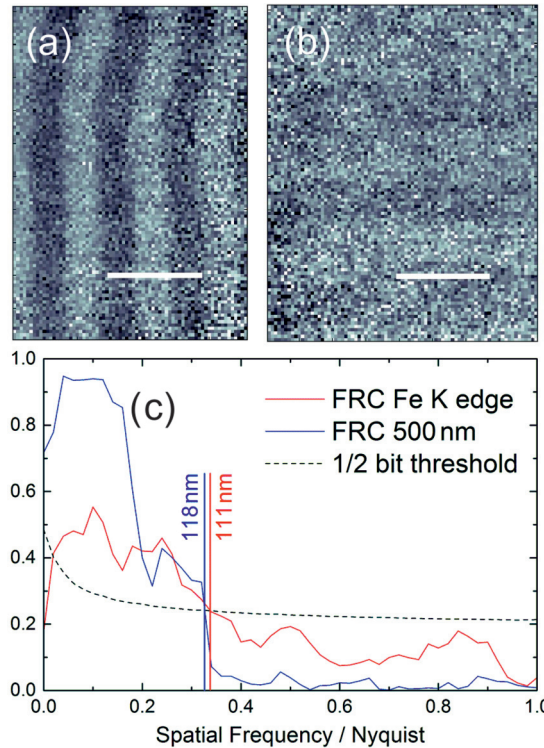

FIG. 5. (a) XMCD absorption image of the magnetic domain structure of the 500 nm FeGd film measured at the Gd L_3 edge. (b) Single polarization absorption image of the 1 μm film measured at the Fe K edge. Scale bars represent 1 μm. (c) The 1/2-bit criterion is used to provide an estimate of the spatial resolution of images [45], which is found to be similar for the two images.

measured for the 1-μm-thick film at the Gd L_3 edge. The relative strengths of the A_{XMCD} signal are shown in Table I. The spatial resolution was determined using a Fourier ring correlation (FRC) method and a profile across the domain boundaries, which was an average of five neighboring line profiles corresponding to a wall length of 200 nm. The Fourier ring correlation curves are shown in Fig. 5(c). It can be seen that the FRC of the image measured at the Fe K edge (red line) is much lower than that of the 500-nm-thick film (blue line) throughout the frequency range, which reflects the lower signal-to-noise ratio of the image of the 1 μm film measured at the Fe K edge. Even though there is a large difference in signal-to-noise ratios, the images were found to have similar spatial resolutions, with the values for each method given in

TABLE I. Comparison of the spatial resolution of different images calculated with Fourier ring correlation (FRC) and edge sharpness (ES) criteria. The strength of the A_{XMCD} signal of each image is normalized to the value of the A_{XMCD} signal at the Fe K edge for ease of comparison.

Thickness	X-ray energy (keV)	A_{XMCD} (a.u.)	FRC (nm)	ES (nm)
1 μm	7.2445 (Gd)	11	45	60
500 nm	7.2430 (Gd)	4	118	120
1 μm	7.1130 (Fe)	1	111	125

Table I. In particular, for the weaker contrast images, the edge sharpness measured with the line profile was reduced to 120 and 125 nm for the thinner film and weaker signal at the Fe *K* edge, respectively, which agrees with the Fourier ring correlation measurements to within 10%.

In summary, we have achieved a spatial resolution of 45 nm with hard x-ray magnetic imaging by means of ptychography. This is a significant advance in the capabilities of x-ray magnetic imaging and will offer access to the magnetic configurations of a wide range of samples. The measurement of high spatial resolution XMCD images at many different sample orientations combined with an appropriate tomographic reconstruction technique will make possible the mapping of the magnetization vector field within micrometer-size magnetic systems with nanoscale resolution. With a few examples of magnetic tomography demonstrated with soft x-ray [7], neutron [11], and electron microscopy [49], this work is therefore a first step towards applying the advantages of hard x rays for tomographic imaging [17] of magnetic systems. Moreover, with future brighter diffraction-limited x-ray sources offering an expected increase in coherent flux of 2–3 orders of magnitude [50,51], hard x-ray dichroic ptychography has the potential to provide single-digit nanometer resolution and be extended towards the investigation of thin-film heterostructures or architectures.

ACKNOWLEDGMENTS

APPENDIX A: SAMPLE CHARACTERIZATION

For image alignment purposes, platinum structures were patterned on the film. These were deposited with focused electron-beam deposition instead of focused ion beam in order to avoid damaging the Si_3N_4 membrane. The magnetic properties of the FeGd films were characterized with magneto-optical Kerr-effect (MOKE) measurements in the polar geometry. The hysteresis loop of the 1-μm-thick film is given in Fig. 6(a). The film has perpendicular magnetic anisotropy with a saturating field of 130 mT. The hysteresis at approximately 100 mT, together with zero remanence at zero field, indicates the spontaneous nucleation and formation of magnetic domains [30,52].

A similarly prepared sample was measured with XMCD fluorescence as a reference for the XMCD results measured with ptychography. To characterize the magnetic properties of the sample, the out-of-plane magnetic hysteresis was investigated by measuring the XMCD signal with x-ray fluorescence as a function of magnetic field applied perpendicular to the sample surface. The hysteresis and nonzero magnetization at
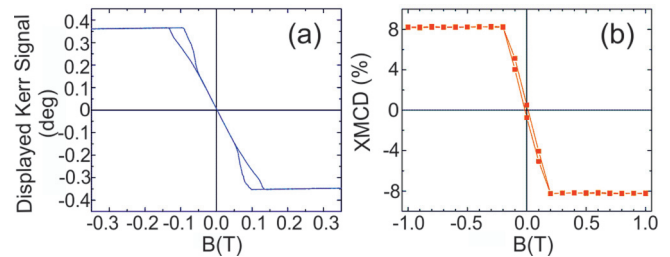

FIG. 6. (a) Out-of-plane hysteresis loop of the 1 μm FeGd multilayer film measured by MOKE in the polar arrangement. (b) The XMCD signal of the reference 1-μm-thick FeGd multilayer film as a function of applied magnetic field, measured by x-ray fluorescence.

remanence indicate that the sample also has an out-of-plane magnetization component.

APPENDIX B: XMCD FLUORESCENCE MEASUREMENTS

X-ray absorption spectroscopy experiments were performed at the ID12 beamline of the European Synchrotron Radiation Facility (ESRF), France at the L_3 edge of Gd and at the *K* edge of Fe using a highly efficient fluorescence yield detection mode in a backscattering geometry [47]. For the XMCD measurements, circularly polarized x rays generated by a helical undulator of the APPLE-II type were used. At these photon energies, the circularly polarized beam emitted by the helical undulator is reduced to 91–92%, due to the partial suppression of horizontal polarization at the Bragg angles of the Si $\langle 111 \rangle$ monochromator. The spectra were corrected for the incomplete circular polarization.

The sample was inserted into the bore of a superconducting magnet. The measurements were carried out at room temperature and under a magnetic field of 1 T applied perpendicular to the sample surface.

XMCD spectra were obtained as a difference of x-ray absorption spectra recorded with right and left circularly polarized x rays. To ensure that the obtained XMCD spectra were free of any experimental artifacts, the data were collected for both directions of the external magnetic field applied parallel and antiparallel to the incoming x-ray beam and the XMCD measurements compared and found to be equivalent.

A reference spectrum for the phase XMCD was calculated using the Kramers-Kronig relations [53] assuming the atomic density of bulk gadolinium (2.38×10^{28} atoms/m^3) and a nominal effective thickness of 520 nm. This was compared with the phase part of the ptychographic XMCD data, ϕ_{XMCD}.

APPENDIX C: PTYCHOGRAPHY EXPERIMENTAL SETUP

X-ray ptychographic imaging was performed at the cSAXS beamline at the Swiss Light Source (SLS), Switzerland with x rays produced by an in-vacuum undulator with 19 mm period, operated at a gap of 5.338 mm. The experiment was performed in air and at room temperature.

The illumination on the sample was defined by a combination of a 35 μm central stop, a gold Fresnel zone plate with 1.2 μm gold thickness, 60 nm outermost zone width, and 170 μm diameter, as well as a 20-μm-diameter order-sorting aperture. The x-ray beam incident on the sample

had a coherent flux of approximately 3×10^7 photons/s and a spot size of 4.5 μm. A diffraction pattern was measured at each of the scanning points with a 0.2 second exposure time using a single-photon counting Pilatus 2M detector [42,43]. To reduce air scattering and absorption, a helium-filled flight tube was placed between the sample and detector. Measurements were taken at 16 energies between 7.234 and 7.2565 keV for the Gd L_3 edge measurements. To enhance the signal-to-noise ratio, 10 such scans were repeated for each energy. These scans were measured with left and right circularly polarized light.

For the Fe K edge measurements, ptychography was performed with C_L polarized x rays only due to time constraints. At 10 energies between 7.109 and 7.118 keV, 60 absorption images were measured and averaged. The quantitative XMCD values were obtained by fitting the histograms of the absorption XMCD contrast of the pixels of the bright and dark magnetic domains to Gaussian distributions and calculating the mean and standard deviation.

APPENDIX D: PTYCHOGRAPHIC RECONSTRUCTIONS

Ptychographic reconstructions were performed with the data from 192×192 pixels of the Pilatus detector, resulting in a reconstruction pixel size of approximately 37 and 38 nm for measurements taken at the Gd L_3 edge and Fe K edge, respectively.

The algorithm initial guess was given by a uniform transmission for the object and an illumination obtained through a previous ptychography measurement on a strongly scattering test object. The initial guess for the illumination was numerically propagated for each different energy in the series to account for the dependence of the Fresnel zone plate focal distance on the photon energy.

The reconstructed images were aligned to a small fraction of a pixel [26] and a linear phase ramp was removed from the images, as in Ref. [54], before the images were averaged.

A smoothly spatially varying phase artifact with an amplitude of a few milliradians was present in the reconstructions. The artifacts varied between different measurements and it is believed that they may arise in the reconstruction as a result of an algorithmic compensation mechanism for small changes in the probe wave front. In order to correct for this artifact, the phase image was projected onto a two-dimensional polynomial orthogonal basis using least-squares fitting similar to that performed in Ref. [55]. An example of this artifact and its subsequent removal is shown in Fig. 7 for a single reconstruction.

After normalization, 10 images for each energy and polarization were averaged, and the A_{XMCD} and ϕ_{XMCD} images were calculated. As discussed in the main text, ptychography assumes a scalar product interaction as follows:

$$\Psi_j(\mathbf{r}) = \mathbf{P}(\mathbf{r})\mathbf{O}(\mathbf{r} - \mathbf{r}_j), \tag{D1}$$

where $\Psi_j(\mathbf{r})$ is the exit field after the sample, $\mathbf{P}(\mathbf{r})$ is the incident illumination, $\mathbf{O}(\mathbf{r} - \mathbf{r}_j)$ is the transmissivity of the sample. These are all complex-valued functions of $\mathbf{r}$, the transverse Cartesian coordinates, and j indicates the ptychography scan position. There is a certain amount of ambiguity when separating the reconstructed probe and object, and the absolute value of the reconstruction is subject to a
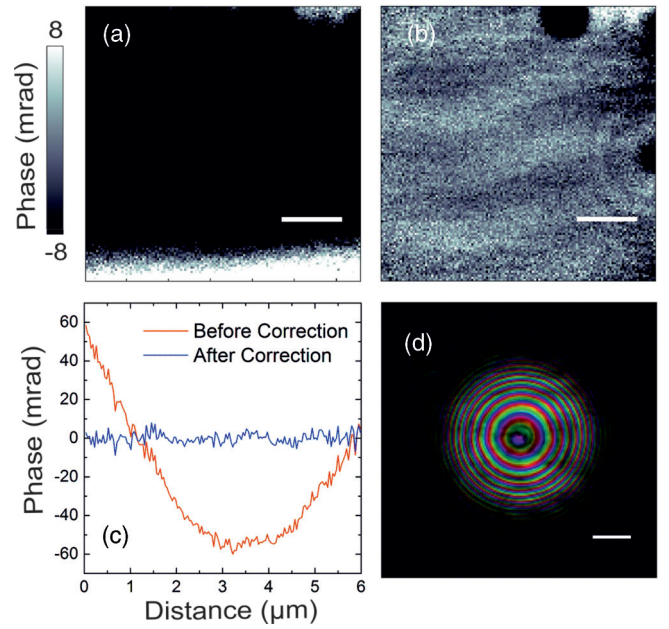

FIG. 7. (a) The smooth phase artifact obscures the fine detail of the image, which is then subtracted to reveal both magnetic and electronic contrast in (b). A line profile taken vertically, both before and after removal of the artifact, is shown in (c), with the background becoming relatively flat after correction. (d) The reconstructed illumination at a photon energy of 7.2430 keV for a scan of the magnetic domains. The amplitude is encoded in the brightness of the image, while the phase of the probe is shown as the hue. Scale bars represent 1 μm.

multiplicative factor D as follows:

$$\Psi_j(\mathbf{r}) = \frac{\mathbf{P}(\mathbf{r})}{D}[\mathbf{O}(\mathbf{r} - \mathbf{r}_j) \cdot D], \tag{D2}$$

which translates to a multiplicative factor for the absorption part, and an additive offset to the phase part of the reconstruction. To obtain the quantitative absorption and absolute phase values, the reconstructions were normalized by removing a phase offset and a multiplicative factor for the phase and absorption parts of the reconstructions, respectively. For a ϕ_{XMCD} image, the average phase of the reconstruction of either helicity was calculated by taking the mean phase value of an equal number of bright and dark domains, and the net offset between the two helicities removed to leave purely magnetic contrast. A value for Δ_{edge} was found from a reference transmission spectrum measured on a similar sample and used to normalize the absorption data. For a sample with an area of air within the image, this ambiguity would be removed by using the air as a reference for normalization.

APPENDIX E: ESTIMATE OF THE XMCD CONTRAST

The expected values for the relative XMCD contrast are given in terms of the real (f_1) and imaginary (f_2) parts of the scattering factor as $\Delta f_1/f_1$ (black line) and $\Delta f_2/f_2$ (red dots) for the Gd L_3 edge and the Fe K edge in Figs. 8(a) and 8(b), respectively. The real part of the scattering factor, f_1, is calculated with the Kramers-Kronig relations from the spectra measured in fluorescence (f_2). This allows the strength of the
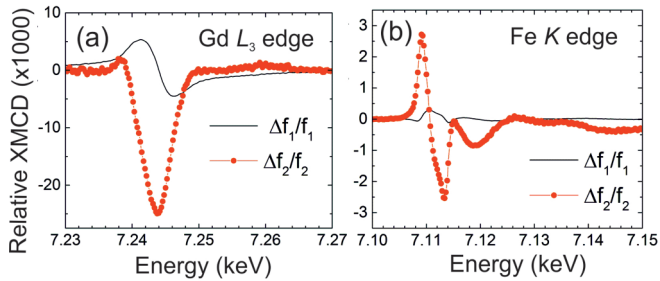
FIG. 8. Comparison of the relative phase ($\Delta f_1/f_1$, black line) and absorption ($\Delta f_2/f_2$, red dots) magnetic contrast (a) across the Gd L_3 edge and (b) across the Fe K edge. At the Fe K edge, it can be seen that the expected phase contrast is much smaller than the absorption contrast.

phase ($\Delta f_1/f_1$) and absorption ($\Delta f_2/f_2$) magnetic contrast at the Gd L_3 and Fe K edges to be compared. The expected absorption magnetic contrast, normalized by the total signal ($\Delta f_2/f_2$), is approximately 10 times weaker at the Fe K edge than the Gd L_3 edge. However, the expected phase magnetic contrast ($\Delta f_1/f_1$) at the Fe K edge is almost 20 times weaker than at the Gd L_3 edge, with a contrast of approximately 0.1 mrad for the 1-μm-thick FeGd film. However, a layer of carbon was deposited on the surface of the film at the region of interest during the experiment due to the sample not being in a vacuum environment. As the phase signal of the carbon deposition ($\geqslant 0.5$ mrad) was greater than the expected ϕ_{XMCD} contrast, it was not possible to extract the ϕ_{XMCD} contrast from the images at the Fe K edge in this experiment.

[1] O. Gutfleisch, M. A. Willard, E. Brück, C. H. Chen, S. G. Sankar, and J. P. Liu, Magnetic materials and devices for the 21st century: Stronger, lighter, and more energy efficient, Adv. Mater. **23**, 821 (2011).

[2] J. Stöhr and H. Siegmann, *Magnetism: From Fundamentals to Nanoscale Dynamics* (Springer, New York, 2006).

[3] J. Stöhr, Y. Wu, B. D. Hermsmeier, M. G. Samant, G. R. Harp, S. Koranda, D. Dunham, and B. P. Tonner, Element-specific magnetic microscopy with circularly polarized x-rays, Science **259**, 658 (1993).

[4] S. Eisebitt, J. Lüning, W. F. Schlotter, M. Lörgen, O. Hellwig, W. Eberhardt, and J. Stöhr, Lensless imaging of magnetic nanostructures by x-ray spectro-holography, Nature (London) **432**, 885 (2004).

[5] C. T. Chen, F. Sette, Y. Ma, and S. Modesti, Soft-x-ray magnetic circular dichroism at the $L_{2,3}$ edges of nickel, Phys. Rev. B **42**, 7262 (1990).

[6] P. Fischer, X-ray imaging of magnetic structures, IEEE Trans. Magn. **51**, 0800131 (2015).

[7] R. Streubel, F. Kronast, P. Fischer, D. Parkinson, O. G. Schmidt, and D. Makarov, Retrieving three-dimensional spin textures by full-field magnetic soft x-ray tomography, Nat. Commun. **6**, 7612 (2015).

[8] P. Fischer, Exploring nanoscale magnetism in advanced materials with polarized x-rays, Mater. Sci. Eng. R **72**, 81 (2011).

[9] F. Pfeiffer, C. Grünzweig, O. Bunk, G. Frei, E. Lehmann, and C. David, Neutron phase imaging and tomography, Phys. Rev. Lett. **96**, 215505 (2006).

[10] B. Betz, P. Rauscher, R. P. Harti, R. Schäfer, H. Van Swygenhoven, A. Kaestner, J. Hovind, E. Lehmann, and C. Grünzweig, In-situ visualization of stress-dependent bulk magnetic domain formation by neutron grating interferometry, Appl. Phys. Lett. **108**, 012405 (2016).

[11] N. Kardjilov, I. Manke, M. Strobl, A. Hilger, W. Treimer, M. Meissner, T. Krist, and J. Banhart, Three-dimensional imaging of magnetic fields with polarized neutrons, Nat. Phys. **4**, 399 (2008).

[12] I. Manke, N. Kardjilov, R. Schäfer, A. Hilger, M. Strobl, M. Dawson, C. Grünzweig, G. Behr, M. Hentschel, C. David, A. Kupsch, A. Lange, and J. Banhart, Three-dimensional imaging of magnetic domains, Nat. Commun. **1**, 125 (2010).

[13] M. R. J. Gibbs, E. W. Hill, and P. J. Wright, Magnetic materials for MEMS applications, J. Phys. D: Appl. Phys. **37**, R237 (2004).

[14] D. Niarchos, Magnetic MEMS: key issues and some applications, Sens. Actuators A Phys. A **109**, 166 (2003).

[15] Y. G. Jiang, S. Masaoka, T. Fujita, M. Uehara, T. Toyonaga, K. Fujii, K. Higuchi, and K. Maenaka, Fabrication of a vibration-driven electromagnetic energy harvester with integrated Nd-FeB/Ta multilayered micro-magnets, J. Micromech. Microeng. **21**, 095014 (2011).

[16] C. Chappert, A. Fert, and F. N. Van Dau, The emergence of spin electronics in data storage, Nat. Mater. **6**, 813 (2007).

[17] M. Holler, A. Diaz, M. Guizar-Sicairos, P. Karvinen, E. Färm, E. Härkönen, M. Ritala, A. Menzel, J. Raabe, and O. Bunk, X-ray ptychographic computed tomography at 16 nm isotropic 3D resolution, Sci. Rep. **4**, 3857 (2014).

[18] F. Hippert, E. Geissler, J. L. Hodeau, E. Leliévre-Berna, and J. R. Regnard, *Neutron and X-ray Spectroscopy* (Springer, New York, 2006).

[19] J. C. Lang, J. Pollmann, D. Haskel, G. Srajer, J. Maser, J. S. Jiang, and S. D. Bader, Imaging buried magnetic domains using hard x rays, Proc. SPIE **4499**, 1 (2001).

[20] K. Sato, Y. Ueji, K. Okitsu, T. Matsushita, and Y. Amemiya, X-ray magnetic circular dichroism imaging with hard x-rays, J. Synchrotron Radiat. **8**, 1021 (2001).

[21] M. Takagaki, M. Suzuki, N. Kawamura, H. Mimura, and T. Ishikawa, IPAP Conf. **7**, 267 (2006).

[22] K. Ueda, A. Nambu, A. Yoneyama, A. Sugawara, S. Heike, T. Hashizume, H. Suzuki, and M. Komuro, Magnetic microstructures of neodymium in $Nd_2Fe_{14}B$ permanent magnet by hard x-ray magnetic-circular dichroism using focused x-ray beam, Appl. Phys. Lett. **97**, 022510 (2010).

[23] M. J. Kramer, R. W. McCallum, I. A. Anderson, and S. Constantinides, Prospects for non-rare earth permanent magnets for traction motors and generators, JOM **64**, 752 (2012).

[24] J. M. Rodenburg, A. C. Hurst, A. G. Cullis, B. R. Dobson, F. Pfeiffer, O. Bunk, C. David, K. Jefimovs, and I. Johnson, Hard-X-Ray Lensless Imaging of Extended Objects, Phys. Rev. Lett. **98**, 034801 (2007).

[25] P. Thibault, M. Dierolf, A. Menzel, O. Bunk, C. David, and F. Pfeiffer, High-resolution scanning x-ray diffraction microscopy, Science **321**, 379 (2008).

[26] M. Guizar-Sicairos and J. R. Fienup, Phase retrieval with transverse translation diversity: A nonlinear optimization approach, Opt. Express **16**, 7264 (2008).

[27] A. M. Maiden and J. M. Rodenburg, An improved ptychographical phase retrieval algorithm for diffractive imaging, Ultramicroscopy **109**, 1256 (2009).

[28] A. Diaz, P. Trtik, M. Guizar-Sicairos, A. Menzel, P. Thibault, and O. Bunk, Quantitative x-ray phase nanotomography, Phys. Rev. B **85**, 020104 (2012).

[29] C. Donnelly, M. Guizar-Sicairos, V. Scagnoli, M. Holler, T. Huthwelker, A. Menzel, I. Vartiainen, E. Müller, E. Kirk, S. Gliga, J. Raabe, and L. J. Heyderman, Element-specific x-ray phase tomography of 3D structures at the nanoscale, Phys. Rev. Lett. **114**, 115501 (2015).

[30] A. Tripathi, J. Mohanty, S. H. Dietze, O. G. Shpyrko, E. Shipton, E. E. Fullerton, S. S. Kim, and I. McNulty, Dichroic coherent diffractive imaging, Proc. Natl. Acad. Sci. USA **108**, 13395 (2011).

[31] A. Scherz, W. F. Schlotter, K. Chen, R. Rick, J. Stöhr, J. Lüning, I. McNulty, Ch. Günther, F. Radu, W. Eberhardt, O. Hellwig, and S. Eisebitt, Phase imaging of magnetic nanostructures using resonant soft x-ray holography, Phys. Rev. B **76**, 214410 (2007).

[32] J. Turner, X. Huang, O. Krupin, K. A. Seu, D. Parks, S. Kevan, E. Lima, K. Kisslinger, I. McNulty, R. Gambino, S. Mangin, S. Roy, and P. Fischer, X-ray diffraction microscopy of magnetic structures, Phys. Rev. Lett. **107**, 033904 (2011).

[33] S. Flewett, C. M. Günther, C. von Korff Schmising, B. Pfau, J. Mohanty, F. Büttner, M. Riemeier, M. Hantschmann, M. Kläui, and S. Eisebitt, Holographically aided iterative phase retrieval, Opt. Express **20**, 29210 (2012).

[34] X. Shi, P. Fischer, V. Neu, D. Elefant, J. C. T. Lee, D. A. Shapiro, M. Farmand, T. Tyliszczak, H.-W. Shiu, S. Marchesini, S. Roy, and S. D. Kevan, Soft x-ray ptychography studies of nanoscale magnetic and structural correlations in thin $SmCo_5$ films, Appl. Phys. Lett. **108**, 094103 (2016).

[35] P. Ferrand, M. Allain, and V. Chamard, Ptychography in anisotropic media, Opt. Lett. **40**, 5144 (2015).

[36] J. P. Hannon, G. T. Trammell, M. Blume, and D. Gibbs, X-ray resonance exchange scattering, Phys. Rev. Lett. **61**, 1245 (1988).

[37] J. P. Hill and D. F. McMorrow, Resonant exchange scattering: polarization dependence and correlation function, Acta Crystallogr. Sect. A **52**, 236 (1996).

[38] S. W. Lovesey and S. P. Collins, *X-ray Scattering and Absorption by Magnetic Materials. Oxford Series on Synchrotron Radiation* (Oxford Science, Oxford, 1996), Vol. 1.

[39] C. Giles, C. Malgrange, J. Goulon, F. de Bergevin, C. Vettier, E. Dartyge, A. Fontaine, C. Giorgetti, and S. Pizzini, Energy-dispersive phase plate for magnetic circular dichroism experiments in the X-ray range, J. Appl. Crystallogr. **27**, 232 (1994).

[40] V. Scagnoli, C. Mazzoli, C. Detlefs, P. Bernard, A. Fondacaro, L. Paolasini, F. Fabrizi, and F. de Bergevin, Linear polarization scans for resonant x-ray diffraction with a double-phase-plate configuration, J. Synchrotron Radiat. **16**, 778 (2009).

[41] X. J. Huang, H. Yan, R. Harder, Y. Hwu, I. K. Robinson, and Y. S. Chu, Optimization of overlap uniformness for ptychography, Opt. Express **22**, 12634 (2014).

[42] B. Henrich, A. Bergamaschi, C. Broennimann, R. Dinapoli, E. F. Eikenberry, I. Johnson, M. Kobas, P. Kraft, A. Mozzanica, and B. Schmitt, PILATUS: A single photon counting pixel detector for x-ray applications, Nucl. Instrum. Methods Phys. Res., Sect. A **607**, 247 (2009).

[43] P. Kraft, A. Bergamaschi, C. Broennimann, R. Dinapoli, E. F. Eikenberry, B. Henrich, I. Johnson, A. Mozzanica, C. M. Schlepitz, P. R. Willmott, and B. Schmitt, Characterization and calibration of PILATUS detectors, IEEE Trans. Nucl. Sci. **56**, 758 (2009).

[44] P. Thibault and M. Guizar-Sicairos, Maximum-likelihood refinement for coherent diffractive imaging, New J. Phys. **14**, 063004 (2012).

[45] M. van Heel and M. Schatz, Fourier shell correlation threshold criteria, J. Struct. Biol. **151**, 250 (2005).

[46] I. Mohacsi, I. Vartiainen, M. Guizar-Sicairos, P. Karvinen, V. A. Guzenko, E. Müller, E. Färm, M. Ritala, C. M. Kewish, A. Somogyi, and C. David, High resolution double-sided diffractive optics for hard X-ray microscopy, Opt. Express **23**, 776 (2015).

[47] A. Rogalev *et al. Magnetism and Synchrotron Radiation*, edited by E. Beaurepaire *et al.* (Springer-Verlag, Berlin, 2001), p. 60.

[48] C. Kittel, Theory of the structure of ferromagnetic domains in films and small particles, Phys. Rev. **70**, 965 (1946).

[49] C. Phatak, Y. Liu, E. Begum Gulsoy, D. Schmidt, E. Franke-Schubert, and A. Petford-Long, Visualization of the magnetic structure of sculpted three-dimensional cobalt nanospirals, Nanoletters **14**, 759 (2014).

[50] M. Eriksson, J. F. van der Veen, and C. Quitmann, Diffraction-limited storage rings - a window to the science of tomorrow, J. Synchrotron Radiat. **21**, 837 (2014).

[51] P. Thibault, M. Guizar-Sicairos, and A. Menzel, Coherent imaging at the diffraction limit, J. Synchrotron Radiat. **21**, 1011 (2014).

[52] A. K. Suszka, A. Etxebarria, O. Idigoras, D. Cortés-Ortuño, P. Landeros, and A. Berger, Field angle dependent change of the magnetization reversal mode in epitaxial Co (0001) films, Appl. Phys. Lett. **105**, 222402 (2014).

[53] B. Watts, Calculation of the Kramers-Kronig transform of x-ray spectra by a piecewise Laurent polynomial method, Opt. Express **22**, 23628 (2014).

[54] M. Guizar-Sicairos, A. Diaz, M. Holler, M. S. Lucas, A. Menzel, R. A. Wepf, and O. Bunk, Phase tomography from x-ray coherent diffractive imaging projections, Opt. Express **19**, 21345 (2011).

[55] E. Lima, A. Diaz, M. Guizar-Sicairos, S. Gorelick, P. Pernot, T. Schleier, and A. Menzel, Cryo-scanning x-ray diffraction microscopy of frozen-hydrated yeast, J. Microscopy **249**, 1 (2013).